Spatially confined quantification of bilirubin concentrations by spectroscopic visible-light optical coherence tomography

COLIN VEENSTRA,* WILMA PETERSEN, IVO M. VELLEKOOP, WIENDELT STEENBERGEN, AND NIENKE BOSSCHAART

Biomedical Photonic Imaging Group, Faculty of Science and Technology, Technical Medical Centre, University of Twente, P.O. Box 217, 7500 AE Enschede, The Netherlands
*c.veenstra@utwente.nl

Abstract: Spatially confined measurements of bilirubin in tissue can be of great value for noninvasive bilirubin estimations during neonatal jaundice, as well as our understanding of the physiology behind bilirubin extravasation. This work shows the potential of spectroscopic visible-light optical coherence tomography (sOCT) for this purpose. At the bilirubin absorption peak around 460 nm, sOCT suffers from a strong signal decay with depth, which we overcome by optimizing our system sensitivity through a combination of zero-delay acquisition and focus tracking. In a phantom study, we demonstrate the quantification of bilirubin concentrations between 0 and 650 µM with only a 10% difference to the expected value, thereby covering the entire clinical pathophysiological range.

OCIS codes: (170.4500) Optical coherence tomography; (300.1030) Absorption.

References and links

1. T. W. Hansen, "Prevention of neurodevelopmental sequelae of jaundice in the newborn," Dev. Med. Child Neurol. **53**(Suppl 4), 24–28 (2011).
2. N. Bosschaart, J. H. Kok, A. M. Newsum, D. M. Ouweneel, R. Mentink, T. G. van Leeuwen, and M. C. Aalders, "Limitations and opportunities of transcutaneous bilirubin measurements," Pediatrics **129**(4), 689–694 (2012).
3. K. Grohmann, M. Roser, B. Rolinski, I. Kadow, C. Müller, A. Goerlach-Graw, M. Nauck, and H. Küster, "Bilirubin measurement for neonates: Comparison of 9 frequently used methods," Pediatrics **117**(4), 1174–1183 (2006).
4. A. Knudsen, "The Cephalocaudal Progression of Jaundice in Newborns in Relation to the Transfer of Bilirubin from Plasma to Skin," Early Hum. Dev. **22**(1), 23–28 (1990).
5. N. Bosschaart, M. C. G. Aalders, D. J. Faber, J. J. A. Weda, M. J. C. van Gemert, and T. G. van Leeuwen, "Quantitative measurements of absorption spectra in scattering media by low-coherence spectroscopy," Opt. Lett. **34**(23), 3746–3748 (2009).
6. F. E. Robles and A. Wax, "Separating the scattering and absorption coefficients using the real and imaginary parts of the refractive index with low-coherence interferometry," Opt. Lett. **35**(17), 2843–2845 (2010).
7. J. Yi, Q. Wei, W. Liu, V. Backman, and H. F. Zhang, "Visible-light optical coherence tomography for retinal oximetry," Opt. Lett. **38**(11), 1796–1798 (2013).
8. J. Yi, W. Liu, S. Chen, V. Backman, N. Sheibani, C. M. Sorenson, A. A. Fawzi, R. A. Linsenmeier, and H. F. Zhang, "Visible light optical coherence tomography measures retinal oxygen metabolic response to systemic oxygenation," Light Sci. Appl. **4**(9), e334 (2015).
9. S. P. Chong, C. W. Merkle, C. Leahy, H. Radhakrishnan, and V. J. Srinivasan, "Quantitative microvascular hemoglobin mapping using visible light spectroscopic Optical Coherence Tomography," Biomed. Opt. Express **6**(4), 1429–1450 (2015).
10. F. E. Robles, C. Wilson, G. Grant, and A. Wax, "Molecular imaging true-colour spectroscopic optical coherence tomography," Nat. Photonics **5**(12), 744–747 (2011).
11. S. Chen, X. Shu, J. Yi, A. Fawzi, and H. F. Zhang, "Dual-band optical coherence tomography using a single supercontinuum laser source," J. Biomed. Opt. **21**(6), 066013 (2016).
12. N. Bosschaart, D. J. Faber, T. G. van Leeuwen, and M. C. G. Aalders, "In vivo low-coherence spectroscopic measurements of local hemoglobin absorption spectra in human skin," J. Biomed. Opt. **16**(10), 100504 (2011).
13. S. Pi, A. Camino, W. Cepurna, X. Wei, M. Zhang, D. Huang, J. Morrison, and Y. Jia, "Automated spectroscopic retinal oximetry with visible-light optical coherence tomography," Biomed. Opt. Express **9**(5), 2056–2067 (2018).
14. S. Yun, G. Tearney, B. Bouma, B. Park, and J. de Boer, "High-speed spectral-domain optical coherence tomography at 1.3 mum wavelength," Opt. Express **11**(26), 3598–3604 (2003).

15. N. Bosschaart, M. C. Aalders, T. G. van Leeuwen, and D. J. Faber, "Spectral domain detection in low-coherence spectroscopy," Biomed. Opt. Express **3**(9), 2263–2272 (2012).
16. N. Bosschaart, D. J. Faber, T. G. van Leeuwen, and M. C. G. Aalders, "Measurements of wavelength dependent scattering and backscattering coefficients by low-coherence spectroscopy," J. Biomed. Opt. **16**(3), 030503 (2011).
17. N. Bosschaart, R. Mentink, J. H. Kok, T. G. van Leeuwen, and M. C. G. Aalders, "Optical properties of neonatal skin measured in vivo as a function of age and skin pigmentation," J. Biomed. Opt. **16**(9), 097003 (2011).

1. Introduction

Bilirubin is the yellow, toxic breakdown product of hemoglobin, which is excreted by the body in bile and urine. Elevated levels of bilirubin lead to jaundice: a yellow discoloration of the eyes and skin. In case of severe jaundice (hyperbilirubinemia), bilirubin can accumulate in the brain and induce kernicterus, which results in irreversible brain damage [1]. Therefore, it is of vital importance to monitor bilirubin levels in high-risk population groups, such as newborns. Unfortunately, current clinically applied methods for bilirubin monitoring are either invasive (blood sampling), or are not accurate enough to fully replace invasive blood sampling (transcutaneous bilirubinometry by diffuse reflectance spectroscopy) [2, 3].

Here, we investigate the use of visible-light spectroscopic optical coherence tomography (sOCT) for noninvasive bilirubin determinations. The unique advantage of sOCT is that it allows for both quantitative and spatially confined measurements of bilirubin concentrations. This potentially enables the noninvasive determination of bilirubin concentrations within blood vessels, facilitating a direct comparison with invasive blood sampling without any cross talk from surrounding tissue. Since the existing transcutaneous bilirubinometers are unable to spatially resolve detected photons, cross talk from surrounding tissue is their main accuracy limiting factor [2]. Another important potential application of sOCT is the noninvasive study of local bilirubin extravasation into skin and brain tissue. As such a study is currently impossible, this may lead to a more fundamental understanding on the development of pathologies like kernicterus [2] and processes like the cephalocaudal progression of jaundice [4].

Multiple studies have shown the feasibility of sOCT and the closely related technology low-coherence spectroscopy (LCS) for the ex vivo [5, 6] and in vivo quantification of absorber concentrations in the visible wavelength range, including preclinical applications for highly localized tissue oximetry [7–13]. Using sOCT for bilirubin quantification in tissue introduces several sensitivity-related challenges, as bilirubin absorbs around the relatively short wavelengths of 440 nm (free bilirubin) and 470 nm (albumin-bound bilirubin). This wavelength region is not only associated with impaired penetration depth into tissue, but also comes with a sharper roll-off of the sensitivity with depth due to the finite pixel size of the detecting spectrograph [14]. Hence, bilirubin determinations require an sOCT system with superior sensitivity, which we realize here by combining spectral domain sOCT with focus tracking and zero-delay acquisition throughout the entire axial scanning range. Besides the optimization of system sensitivity, this also ensures that the measured attenuation is only affected by the sample itself, resulting in quantitative measurements of the optical properties of the sample without requiring any calibration procedure.

In this work, we validate our sOCT system in the wavelength range of 440-600 nm for quantitative bilirubin determinations in samples mimicking neonatal skin. We show that our sOCT method is able to estimate bilirubin concentrations up to 650 µM with an accuracy of 10% and a standard deviation in the order of 50 µM. The investigated bilirubin range covers the entire clinical pathophysiological range (50 – 500 µM) [2, 3]. To demonstrate the spatially confined aspect of the technique, we also measured bilirubin concentrations behind an epidermis mimicking scattering layer with an accuracy of 10%.
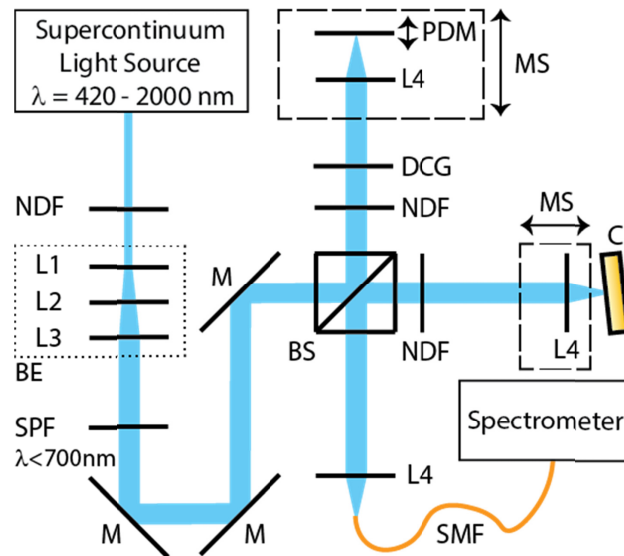
2. Methods

2.1 Setup

Fig. 1. Schematic overview of the sOCT setup. NDF: neutral density filters, L#: lens #, BE: beam expander, SPF: short pass filter, M: mirror, BS: beam splitter, DCG: dispersion compensation glass, MS: motorized stage, PDM: piezo driven mirror, C: cuvette with sample, SMF: single mode fiber.

Our sOCT setup (Fig. 1) is based on an open air Michelson interferometer, with a supercontinuum light source (SuperK EXTREME EXB-6, NKT Photonics, Denmark). Two neutral density filters (ND05A, Thorlabs, USA) attenuate the light (Total optical density = 1). Three lenses (LD2746-A, LD2060-A, LB1471-A, Thorlabs, USA) expand and collimate the beam, resulting in a beam with a diameter of 3 mm (full width at half maximum). A short pass filter (FESH0700, Thorlabs, USA) filters out all wavelengths longer than 700 nm. Protected silver mirrors (PF10-03-P01, Thorlabs, USA) guide the beam into the desired direction. A 10:90 beam splitter (BS028, Thorlabs, USA) guides 10% of the light towards the sample arm and 90% towards the reference arm. In both, the sample arm (NDC-50C-2M-A, Thorlabs, USA) and the reference arm (NDC-50C-4M, Thorlabs, USA), the light intensity can be controlled by variable neutral density filters. Achromatic lenses (AC127-025-A, Thorlabs, USA) with a focal length of 25 mm focus the light on the sample contained by a glass cuvette, and a piezo-driven oscillating reference mirror. A motorized linear stage (T-LS13M, Zaber, USA) controls the reference arm length by joint translation of the reference mirror and its focusing lens. An identical stage facilitates focus tracking by translation of the focusing lens in the sample arm (see section 2.2.3). The back scattered light from both arms is guided by a single mode fiber (S405-XP, Thorlabs, USA) to a home-built spectrometer, where it is dispersed by a grating on a line scan camera (Sprint spL4096-140km, Basler, Germany) with a spectral resolution $\delta\lambda = 0.1$ nm over a range of 440-600 nm. This results in a theoretical axial resolution of 1.4 μm in air.

2.2 Data acquisition and processing

A schematic overview of data acquisition and processing is shown in Fig. 2. The optical path length difference between the sample and the reference arm $\Delta OPL = 2n(x_s - x_r)$, with n the refractive index of the sample, and x_s and x_r the sample arm length and reference arm length respectively, induces a modulation on the detected intensity I_{det}:

$$I_{det}(\lambda,t) \propto I_s(\lambda) + I_r(\lambda) + \sqrt{I_s(\lambda)I_r(\lambda)}\left(e^{i\frac{2\pi}{\lambda}\Delta OPL(t)} + e^{-i\frac{2\pi}{\lambda}\Delta OPL(t)}\right) \qquad (1)$$

where I_s and I_r are the signal intensities from the sample arm and reference arm, respectively.
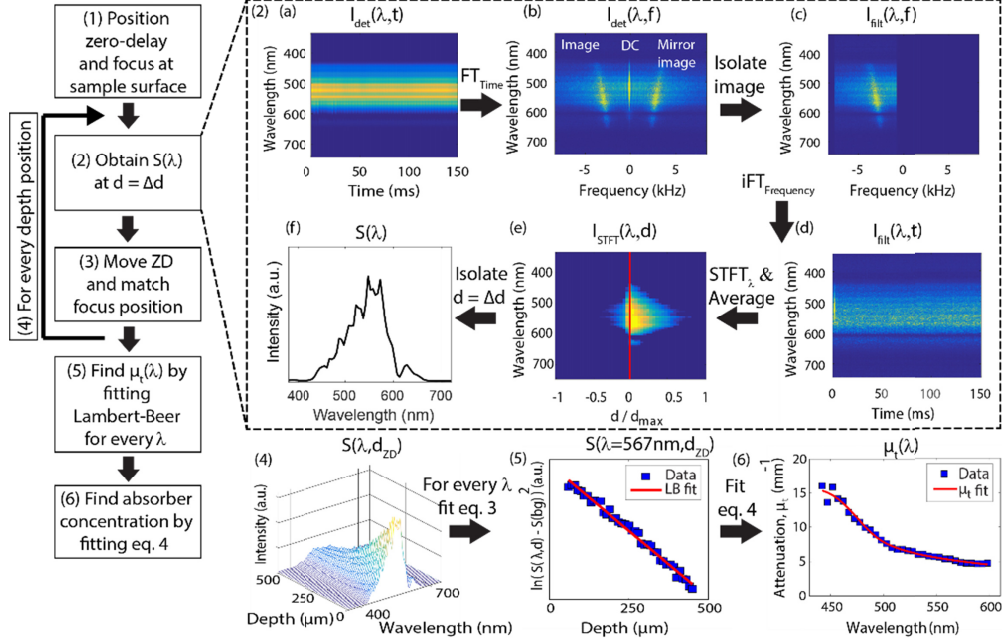

Fig. 2. Schematic overview of the data acquisition and processing as performed in this study. All numbers and letters within parentheses denote the data processing steps that are explained in section 2.2. For all data sets containing complex data (2 b-d), only the absolute values are shown. ZD: zero-delay, LB: Lambert-Beer.

2.2.1 Zero-delay acquisition

The finite spectral resolution of the detecting spectrograph results in a sensitivity roll-off as a function of depth [14]. To optimize our system sensitivity, we apply zero-delay acquisition along the full axial range, i.e. at any depth inside the sample. Hereto, we apply the method described in our previous work to remove the undesired crosstalk between the OCT signal and its mirror image [15]. In short, a piezo-driven saw-tooth movement of the reference mirror induces a modulation of ΔOPL as a function of time with frequency $f_D = 2v_r/\lambda$, where v_r is the velocity of the moving reference mirror (0.85 mm/s). The change in ΔOPL is limited to 5 µm by acquisition of only 50 lines (exposure time: 50 µs per line, linerate: 16.7 kHz) per period of the piezo-driven movement (100 ms). Triggering of the camera by reference mirror position ensures that for every period, acquisition is performed over the same part (at which the movement speed is constant) of the piezo-driven movement. Acquisition of a total of N = 2500 lines takes 5 seconds and results in a data set $I_{det}(\lambda,t)$ (Fig. 2, step 2a). Fourier transformation of $I_{det}(\lambda,t)$ with respect to time results in the frequency content of the signal $I_{det}(\lambda,f)$, containing the frequency of the modulation of ΔOPL as a result of the reference mirror movement (Fig. 2, step 2b). The DC component and the positively shifted frequencies (mirror-image) are removed from $I_{det}(\lambda,f)$ by a rectangular bandpass filter around the negatively shifted frequencies (−7.3 to −0.4 kHz) (Fig. 2, step 2c). Inverse Fourier transformation of the filtered frequency content with respect to frequency results in the filtered intensity $I_{filt}(\lambda,t)$, with the DC component and mirror image removed (Fig. 2, step 2d):

$$I_{filt}(\lambda,t) \propto \sqrt{I_s(\lambda)I_r(\lambda)}e^{-i\frac{2\pi}{\lambda}\Delta OPL(t)} \qquad (2)$$

2.2.2 Short time Fourier transformation

For the purpose of quantitative and spatially confined spectroscopy, we are interested in I_s as a function of both wavelength and geometrical depth d, with $d = \Delta OPL/(2n)$. Since $I_{filt}(\lambda,t)$ contains the spectral content of the OCT signal over the entire imaging range of the spectrograph ($d_{max} = 622$ µm), the spectra are not yet spatially confined at each depth. Short time Fourier transformation (STFT) of $I_{filt}(\lambda,t)$ with respect to λ with a rectangular spectral window with a size of $\Delta\lambda = 5$ nm, results in a depth-resolved spectral data set $I_{STFT}(\lambda,d,t)$ with a spatial resolution $\Delta d = \lambda^2/(2n\Delta\lambda)$ ranging between 14 µm (at $\lambda = 440$ nm) and 27 µm (at $\lambda = 600$ nm). The STFT is applied directly in the wavelength domain, since an interpolation filter to convert data to the equidistant wave number domain has its own frequency characteristics which affect depth information and thus affects quantitative analysis. Averaging of $|I_{STFT}(\lambda,d,t)|$ with respect to time (i.e. for every line captured by the camera) yields $I_{STFT}(\lambda,d)$ (Fig. 2, step 2e). Since I_r remains constant during the complete measurement, $I_{STFT}(\lambda,d)$ contains the depth profile of $\sqrt{I_s}$ per wavelength, from which we obtain $S(\lambda) = I_{STFT}(\lambda,d = \Delta d)$ (Fig. 2, step 2f). The backscattered spectrum at $d = \Delta d$ is used, since it has a better signal-to-noise ratio compared to the backscattered spectrum at $d = 0$ (i.e. exactly at zero-delay), due to small remainders of the DC term after filtering.

2.2.3 Focus tracking and depth-resolved acquisition

In addition to zero-delay acquisition, we further optimize our system sensitivity by focus tracking. At the start of each measurement, the zero-delay and focus position are matched at the interface between the cuvette wall and the sample (Fig. 2, step 1). Subsequently, $S(\lambda,d_{ZD})$ is obtained by acquisition of $S(\lambda)$ as a function of the zero-delay (ZD) position relative to the sample's surface d_{ZD}, with step size dx and the method described in sections 2.2.1 and 2.2.2. Hereto, the reference arm is elongated with steps of $dx \cdot n$ and focus tracking is achieved by translating the sample lens with steps dx/n towards the sample (Fig. 2, step 3). This method for combined zero-delay acquisition and focus tracking results in a depth resolved and wavelength resolved OCT signal $S(\lambda,d_{ZD})$, from which the attenuation in depth only depends on the optical properties of the sample (Fig. 2, step 4).

2.2.4 Spectra of optical properties

Under the assumption of single scattering, the attenuation coefficient $\mu_t(\lambda)$ of the sample is obtained by fitting a linear Lambert-Beer model to the natural logarithm of $S(\lambda,d_{ZD})$ (Fig. 2, step 5):

$$\ln\left((S(\lambda,d_{ZD}) - S_{bg})^2\right) = \ln(\alpha(\lambda)) - 2\mu_t(\lambda)d_{ZD} \tag{3}$$

with $\alpha(\lambda)$ and $\mu_t(\lambda)$ free running fit parameters, and S_{bg} a background term that is obtained at a depth of 1000 µm inside the non-scattering back wall of the sample containing cuvette.

The individual contributions of the scattering coefficient $\mu_s(\lambda)$ (modeled as a scatter power function $a\lambda^{-b}$) and the absorption coefficient $\mu_a(\lambda)$ to the total sample attenuation $\mu_t(\lambda)$ are obtained by fitting Eq. (4) to $\mu_t(\lambda)$, according to our method in [12] (Fig. 2, step 6):

$$\mu_t(\lambda) = a\lambda^{-b} + \sum C_i \mu_{a,i}(\lambda) \tag{4}$$

with fit parameters: scaling factor a, scatter power b, and C_i the concentration of the ith chromophore relative to the chromophore concentration at which the reference absorption spectrum $\mu_{a,i}(\lambda)$ was measured. The lower boundaries of all fit parameters were set to 0. We obtained all $\mu_{a,i}(\lambda)$ by transmission spectroscopy (UV-2401PC, Shimadzu, Japan), comprising the absorption spectra for free bilirubin and albumin-bound bilirubin.

To validate the measured attenuation spectra, the theoretical Mie scattering coefficient spectrum [16] is calculated and compared to the attenuation spectra as measured by our system.

2.3 Tissue mimicking samples

To validate our method, we created a series of aqueous samples ($n = 1.35$) mimicking neonatal skin ($\mu_s \approx 9$ mm^{-1}, assuming an anisotropy of $g = 0.8$) [17] containing NIST certified polystyrene spheres (400nm diameter, 2.5mg/ml solution, Thermo Scientific, USA), a physiological concentration of 40 mg/ml bovine serum albumin (Sigma-Aldrich, Germany), and bilirubin concentrations varying between 0 and 650 μM (Sigma-Aldrich, Germany). Bilirubin was dissolved in DMSO, resulting in a 14mM stock solution, prior to adding it to the rest of the sample. A 200 mM Tris HCl (pH = 8.4) solution was used to dilute the bilirubin to its final concentration. The samples were measured over a depth interval of $d = 0$-500 μm inside the sample ($dx = 10$ μm).

To demonstrate the spatially confined aspect of our sOCT method and to show that the sensitivity of our system is also sufficient to obtain accurate results at larger probing depths, we measured the attenuation of a 335μM bilirubin-polystyrene sample over a depth interval of 0-200 μm ($dx = 2$ μm) behind a scattering silicone layer containing 0.1% TiO$_2$ ($n = 1.47$, $\mu_s \approx 5$ mm^{-1}, thickness = 150 μm, optical density ≈0.33), which mimics the optically homogeneous upper part of the neonatal dermis [17], or adult epidermal skin layer ($\mu_s \approx 4$-8 mm^{-1}, thickness ≈100-150 μm) [12].
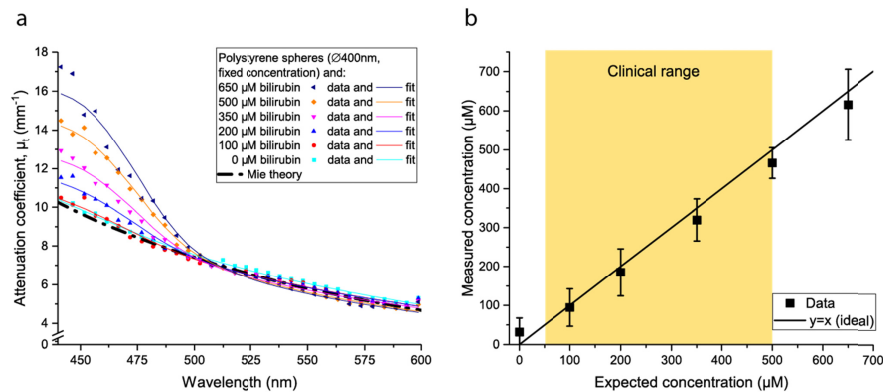
3. Results

Fig. 3. a. Average attenuation spectra μ$_t$(λ) for the samples with a fixed concentration of polystyrene spheres and varying bilirubin concentrations in the clinical pathophysiological range. Mie theory was used to estimate the theoretical scattering coefficient spectrum. Fits are obtained by fitting Eq. (4) to μ$_t$(λ). Error bars (± 10%) are not shown for visibility reasons. b. Estimated bilirubin concentrations (average of 3 measurements, error bars represent standard deviations). Except for the 0 μM bilirubin sample, all averaged values agree within 10% to the expected values. The results cover the full clinical pathophysiological range (indicated by the yellow box).

The measured attenuation spectra $\mu_t(\lambda)$ for the polystyrene/bilirubin samples are shown in Fig. 3(a) (average of 3 measurements), along with the fits obtained by fitting Eq. (4) to $\mu_t(\lambda)$. The attenuation for wavelengths that are absorbed by bilirubin ($\lambda < 525$ nm) increases linearly with bilirubin concentration. The theoretical Mie scattering coefficient spectrum of the polystyrene spheres (dash-dotted black line in Fig. 3(a)) is in excellent agreement with the non-absorbing 0 μM bilirubin sample, as well as the other samples for $\lambda > 525$ nm.

Figure 3(b) shows the bilirubin concentrations that we derived by fitting Eq. (4) to the measured $\mu_t(\lambda)$. Except for the 0 μM bilirubin sample, all average values agree within 10% with the expected values.
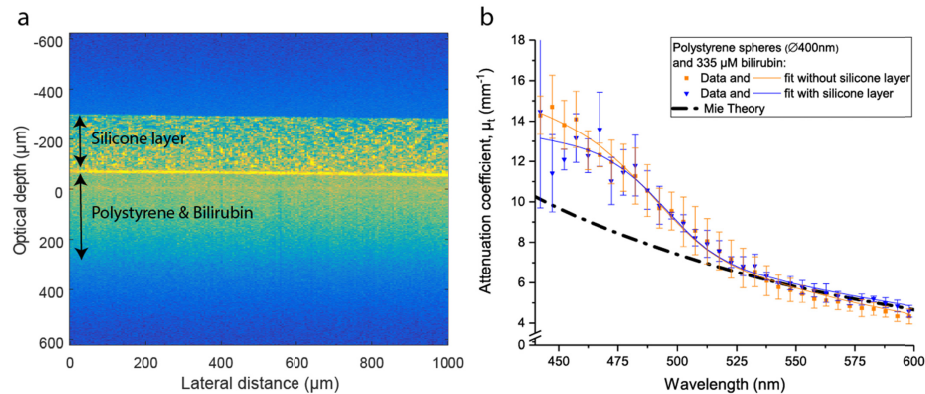

Fig. 4. a. OCT image used to discriminate between the silicone layer and the sample. b. Attenuation spectra $\mu_t(\lambda)$ for the 335μM bilirubin sample with and without the silicone layer (average of 3 measurements). Fits are obtained by fitting Eq. (4) to $\mu_t(\lambda)$. Mie theory was used to estimate the theoretical scattering coefficient spectrum.

Figure 4(a) shows the OCT image of a 335 μM bilirubin-polystyrene sample behind the scattering TiO_2-silicone layer. From this image, we determined the depth of the bilirubin phantom layer, after which the optical attenuation spectrum was obtained using the same procedure of depth acquisition and temporal averaging as for the non-layered phantoms. The sample's attenuation spectrum $\mu_t(\lambda)$ was measured with and without coverage by the silicone layer, as shown in Fig. 4(b) (average of 3 measurements). For $\lambda > 460$ nm, the measured attenuation spectrum behind the silicone layer is in good agreement with the measured attenuation spectrum of the sample without the silicone layer. Again, both attenuation spectra show excellent agreement with the theoretical Mie scattering spectrum for $\lambda > 525$ nm.

Fitting Eq. (4) to the measured attenuation spectra (solid lines, Fig. 4(b)) results in bilirubin concentrations of 310 ± 41 μM and 326 ± 46 μM (mean ± std of 3 measurements) with, and without coverage by the silicone layer, respectively. Both concentrations agree within 10% with the expected bilirubin concentration of 335 μM.

4. Discussion and conclusion

In this study, we have demonstrated the potential of visible-light sOCT to quantify bilirubin concentrations over the complete clinical pathophysiological range (50-500 μM) in neonatal skin mimicking samples. Besides a good agreement between the measured and expected bilirubin absorption of our samples, we also obtained good agreement between the measured optical scattering and Mie theory. With that, we have taken the first steps towards spatially confined measurements of bilirubin concentrations in tissue.

At the bilirubin absorption peak around 460 nm, our sOCT method effectively overcomes the problem of a sharp roll-off of the system sensitivity with depth (−13 dB for the spectrograph's sensitivity at a depth of 500 μm in a sample with n = 1.35), by applying zero-delay acquisition and focus tracking. Compared to other STFT-based methods for sOCT [6–11], our technique has the disadvantage of an increased measurement time. Our method requires acquisition of sufficient (~50) lines to sample the movement of the piezo driven reference mirror, hence measurement time is limited by the reference mirror speed. The measurement time of our method also scales linearly with the depth interval over which we derive the attenuation coefficient by fitting Eq. (3). In this study, data was acquired at a

minimum of 50 depth positions, resulting in a minimum measurement time of 250 seconds for a full data set. For potential future *in vivo* measurements, it is likely that motion artefacts occur within this measurement time, hampering both the quantitative, and localized analysis of the optical attenuation. Measurement time can be reduced by a) reducing the period of the reference mirror movement, b) decreasing the number of averages per depth position, and c) increasing axial step size *dx* or, depending on the application, reducing the depth range to a spatially even more confined region of interest. Options b) and c) potentially come at the cost of measurement accuracy.

For the sample measurement behind the scattering silicone layer, the measured $\mu_t(\lambda)$ is lower and has larger standard deviations than the $\mu_t(\lambda)$ measured without the layer for wavelengths <460 nm (Fig. 4(b)). This can be caused by a) a lower signal to noise ratio inside the sample, due to the increased attenuation by the scattering silicone layer in this spectral region, and b) the influence of multiple scattering on the signal at increasing measurement depths. The presence of multiple scattering results in a lower scattering contribution when fitting Eq. (4) to the measured $\mu_t(\lambda)$ [16]. Since absorption is not affected by the influence of multiple scattering [5], we still obtain approximately the same absorption contribution – and thus bilirubin concentration – compared to the measurement without the covering layer. Nevertheless, when translating this method to spatially confined measurements in tissue, a thorough investigation is required of the measurement accuracy as a function of depth and tissue optical density.

For all samples containing bilirubin, the averaged bilirubin concentration measurements agree within 10% of the expected values. The overestimation of the bilirubin concentration in the 0 µM bilirubin sample may be explained by the lower boundary of 0 for all fit parameters in Eq. (4), resulting in a positive bias for samples containing no or very little bilirubin. Since the standard deviation of the data is in the order of 50 µM, the precision of our method is lower than its accuracy. This precision is comparable to the precision of transcutaneous bilirubinometers for concentrations up to 200 µM [3]. Transcutaneous bilirubinometers however, systematically underestimate the clinically relevant bilirubin concentrations higher than 200 µM [3], whereas the accuracy of our method remains relatively constant for the full investigated range. Furthermore, sOCT has the ability of spatially confining the measurement volume to a small region of interest inside tissue. This can be of great value to I) study the physiological process of bilirubin extravasation into tissue, and II) noninvasively measure bilirubin concentrations inside blood vessels. The latter would overcome the intrinsic accuracy-limiting factor of current transcutaneous bilirubinometers, as these measure the bilirubin concentration in a relatively large skin volume, which does not correlate directly to the bilirubin concentration in blood [2]. Further research is required to investigate whether sOCT can accurately measure bilirubin concentrations in blood where new challenges such as tissue dynamics, especially perfusion, and high hemoglobin absorption ($\mu_a \approx 20$ mm^{-1}) around the same wavelengths as the bilirubin absorption peak arise.

Disclosures

The authors declare that there are no conflicts of interest related to this article.